Muhammad Jawad Munawar[1]
Institute of Geology,
University of the Punjab,
Lahore 54590, Pakistan;
School of Geosciences,
China University of Petroleum,
Qingdao 266580, China;
Department of Earth Sciences,
Khalifa University,
P.O. Box 127788,
Abu Dhabi, UAE
e-mail: jawad.geo@pu.edu.pk

Sandra Vega
Centro de Geociencias,
Campus Juriquilla, UNAM,
Boulevard Juriquilla 3001,
Queretaro, Qro 76230, Mexico;
Department of Earth Sciences,
Khalifa University,
P.O. Box 127788,
Abu Dhabi, UAE
e-mail: sandravega@geociencias.unam.mx

Chengyan Lin
School of Geosciences,
China University of Petroleum,
Qingdao 266580, China
e-mail: lincy@upc.edu.cn

Mohammad Alsuwaidi
Department of Earth Sciences,
Khalifa University,
P.O. Box 127788,
Abu Dhabi, UAE
e-mail: mohammad.alsuwaidi@ku.ac.ae

Naveed Ahsan
Institute of Geology,
University of the Punjab,
Lahore 54590, Pakistan
e-mail: naveedahsan.geo@pu.edu.pk

Ritesh Ramesh Bhakta
Petroleum Institute,
Khalifa University,
P.O. Box 127788,
Abu Dhabi, UAE
e-mail:ritesh.bhakta@msn.com

Upscaling Reservoir Rock Porosity by Fractal Dimension Using Three-Dimensional Micro-Computed Tomography and Two-Dimensional Scanning Electron Microscope Images

Scaling porosity of sedimentary rocks from the scale of measurement to the scale of interest is still a challenge. Upscaling of porosity can assist to accurately predict other petrophysical properties of rock at multiple scales. In this study, we use the two-dimensional (2D) scanning electron microscope (SEM) and three-dimensional (3D) X-ray micro-computed tomography (micro-CT) image to upscale porosity from the image scale to the core plug scale. A systematic imaging plan is deployed to capture rock properties of a carbonate and a sandstone sample, which are sensitive to the fractal nature of these rocks. Image analysis records wider pore spectrum (0.12–50 μm) in the carbonate sample than in sandstone (0.12–30 μm). The fractal dimensions are also higher in the carbonate than in the sandstone sample. Median, volume-weighted average of pore radius, and fractal dimensions derived from the image analysis are used as inputs in this equation. The results of the present study using this equation yielded to the best results on a resolution of 2.5 μm/voxel in the sandstone and 2.01 μm/voxel resolution in the carbonate sample for 3D micro-CT images, where fractal-scaling porosity matches well with the porosity measured at the core plug scale. The 2D SEM images provided a good estimation of porosity in the sandstone sample, where micro-CT imaging techniques could not capture the full pore spectrum. The fractal porosity equation showed promising results and offers a potential alternative way to estimate porosity when there are no routine core measurements available.
[DOI: 10.1115/1.4047589]

Keywords: porosity, fractal dimension, micro-CT, SEM, pore size distribution (PSD), geothermal energy, hydrates/coal bed methane/heavy oil/oil sands/tight gas, oil/gas reservoirs, unconventional petroleum, underground injection and storage

1 Introduction

The heterogeneity in natural rocks prevails at a wide range of length scales from microns to kilometers. Practically, the rocks can be considered as arbitrary two-phase systems of the pore and solid phases. Dealing with the pore phase is critical because it is composed of multiscale, complex, and irregular microstructures. Especially, the complexity in sedimentary rocks gets more complicated where a wide variety of deposition and diagenetic process have governed their rock fabric. Accurate quantification of the pore space across several scales in heterogeneous rocks is a significant challenge for oil and gas recovery, transport of groundwater, and pollutant migration in aquifers. Euclidean dimension (D_E) has restraints to explain and compute complex tortuous pore geometries in simple two or three-dimensions [1–4]. Mandelbrot [1] proposed that fractal geometry provides effective means to characterize the multiscale and self-similar geometries, which is an applicable approach to upscale porosity from small scale to large scales in natural rocks. According to this theory, the self-similar objects are composed of similar structures at different scales. To better understand the concept of fractal dimension, let us compare basic concepts in the Euclidean geometry with their analogous in

[1]Corresponding author.

Contributed by the Petroleum Division of ASME for publication in the JOURNAL OF ENERGY RESOURCES TECHNOLOGY. Manuscript received July 25, 2019; final manuscript received May 26, 2020; published online July 28, 2020. Assoc. Editor: Ray (Zhenhua) Rui.

the fractal geometry: The Euclidean dimension (D_E) of a straight line is equal to 1 ($D_E = 1$), while the dimension of an irregular line or a surface presenting self-similar structures is a fraction number larger than 1 and less than 2 [5,6]. The Euclidean dimension of a volumetric object is equal to 3, while the dimension of an irregular tridimensional object that presents self-similarity is a fraction between larger than 2 and less than 3. This provides a fractional sense to a dimension which is known as fractal dimension (D_O). Fractal dimension quantifies irregularity of self-similar structures at different scales.

In the case of rocks, we find the considerable literature that shows that rocks can be described/characterized using fractal geometry. For instance, in a microstructure study of sedimentary rocks by small-angle neutron scattering, Wong et al. [7] concluded that the fractal character of pore surfaces is due to the presence of clays. Analyzing scanning electron microscope (SEM) images of sedimentary rocks, Krohn [8] indicated that the fractal structures are the product of diagenesis. Katz and Thompson [2] experimented on a set of sandstone samples and they proposed a relation between fractal dimension, porosity, and scales of self-similarity. They found that pore spaces in these sandstones are fractals across three or four orders of scale magnitude covering 1 nm to 100 μm. Since then, this fractal geometry theory has drawn huge attention regarding its application in various restraints such as porous media, fractures and vein studies, surface roughness, and granular materials. Many scientists [8–16] have worked on different techniques to find fractal behavior of pore space in sandstone and carbonate rocks, and their results showed that pore space in these sedimentary rocks exhibits obvious fractal nature.

Several methods are in use to determine the fractal dimension and pore size distribution (PSD) of porous rocks such as wetting phase saturation and capillary pressure [17–20] mercury injection capillary pressure (MICP), porous plates and centrifuges [9,13], adsorption and nuclear magnetic resonance method (NMR) [21–24]. Long ago, Katz and Thompson [2], Krohn and Thompson [25], and Krohn [8,26] used two-dimensional (2D) SEM images for the first time to investigate the fractal dimension of sandstone, shale, and carbonate samples. Few studies exist that use the three-dimensional (3D) computed tomography (CT) image to determine fractal dimension [10,27].

Recently, Vega and Jouini [14] made fractal and multifractal analysis on an optical microscope and SEM images, examined the relation of magnification to fractal dimension, and derived a new equation for scaling porosity. This equation utilizes pore size with the approximation that the majority of the pore size is similar and fractal dimensions measured on digital images from SEM and thin section. The evaluation of this equation indicates the potential to estimate porosity at different scales and an alternative way to determine porosity from images.

In this paper, we used high-resolution SEM image mosaics and micro-CT images at different scales to determine PSD, image porosity, and fractal dimensions to calculate fractal-scaling porosity using Vega's equation [14]. We studied the applicability of this fractal-scaling porosity equation on multiscale large area 2D SEM and 3D micro-CT images from a sandstone and a carbonate rock. This is the first time when such equation is used to calculate fractal-scaling porosity of both 2D and 3D digital images from two types of rocks (siliciclastic and carbonate) having similar porosities. In this way, this study adds to the original paper [14] the investigation of the scaling porosity equation using 3D images and its test in a sandstone sample.

2 Methods and Materials

2.1 Fractal-Scaling Porosity Equation. A simple empirical relation can be drawn by plotting image resolution versus image porosity computed to scale porosity for multiple scales. Whereas porosity computed by images is dependent on resolution, magnification, and artifacts, thus true relation cannot be revealed at that multiple scale's relationship. Fractal objects are independent of the measurement units (length, area, or volume) and follow a scaling law. Katz and Thompson [2] proposed an alternative scaling law (1) to calculate porosity using fractal geometry

$$\Phi = \left(\frac{L_1}{L_2}\right)^{(D_E - Do)} \tag{1}$$

where L_1 is minimum and L_2 is the maximum length of the fractal structure, these are also referred as the lower and upper limits of the self-similar structure; Do is the fractal dimension of the pore space, and D_E is the Euclidian dimension. In this case, as Do approaches D_E, the pore space tends to be Euclidian, resulting in a fractal porosity equal to 1 ($\Phi = 1$). In other words, a fractal porosity equal to 1 indicates that L_1 is equal to L_2, so there is not a fractal structure. L_1 can be assumed as 20 deg A, which is a minimum size of a crystal nucleus of pore space in siliciclastic rocks. L_2 yet to be found for each specific structure. Some workers tried to establish a correlation function in images to find L_2, but the scope of this function might be narrow and limited to measured scales [28]. Therefore, for calculating porosity at multiple scales (1), results are not relevant.

The porosity estimation from images can simply be calculated by dividing the pore area by the total image area (2) in 2D images, and the pore volume by the total pore volume (3) in 3D images

$$\Phi = \frac{AP}{AT} \tag{2}$$

$$\Phi = \frac{VP}{VT} \tag{3}$$

where A_P is the pore area, A_T is the total area of a 2D image, V_P is the pore volume, and V_T is the total volume of a 3D image.

The box-counting method is used by many authors [12,29,30] to find fractal dimensions of binary images. The principle of this method is to count the number of boxes $N(\epsilon)$ covering the pore spaces by superimposing boxes with the box size ϵ onto an image. The process is iterated in a series of decreasing caliber of box sizes. $N(\epsilon)$ and ϵ should satisfy Eq. (4) if the pore space is fractal in nature

$$N(\varepsilon) = \varepsilon^{-Do} \tag{4}$$

For 2D images, Vega and Jouini [14] derived Eq. (5) from Eq. (3) by assuming that the pore size is determined by the box(es) that covers the pore of dimension $e \times e$, where e is the pore size; they defined dimensionless pore size, $e' = e/L$, where L is taken as the length of square of image. A dimensionless image size can be given as $L' = L/L$ which will be equal to 1. They also define dimensionless pore area $a_p = e' \times e'$ and dimensionless image area $AT' = L' \times L'$.

$$\Phi = \frac{AP}{AT} = \frac{N(\varepsilon) \times a_P}{AT'} \tag{5}$$

Now, substituting Eq. (4) in Eq. (5) and approximating the box size ϵ near to pore size e', such that $\epsilon \approx e'$

$$\Phi = \frac{\varepsilon^{-Do} \times ap}{AT'} \tag{6}$$

$$\Phi = \frac{e'^{-Do} \times ap}{AT'} = e'^{(DE - Do)} \tag{7}$$

So, we used Eq. (7) to estimate the fractal-scaling porosity in 2D images, where D_E is equal 2, and assuming that most the pores are equal in size.

Following the same reasoning of above, now for 3D cubical images. This is, instead of having a square image, we have a

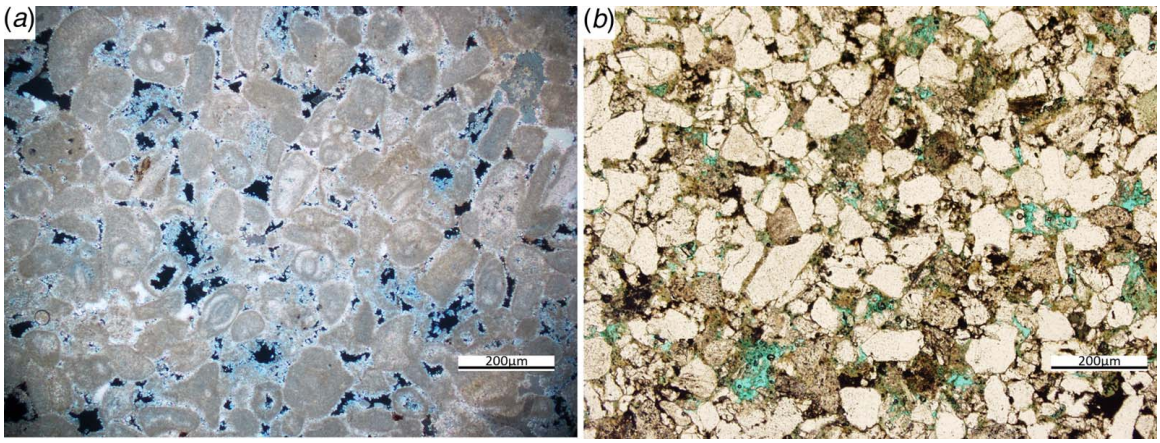

Fig. 1 Thin section photomicrographs of rock samples used in this study: (*a*) carbonate (G3) and (*b*) shaly-sandstone (ES3-1)

cubical image of $L \times L \times L$ of total volume. Then, Eq. (7) becomes Eq. (8) for 3D images

$$\Phi = \frac{e'^{-Do} \times \text{vp}}{\text{VT}'} = e'^{(DE-Do)} \tag{8}$$

where e' is the dimensionless pore size, vp is the dimensionless pore volume ($\text{vp} = \text{e}' \times \text{e}' \times \text{e}'$), VT′ is the dimensionless total volume of a 3D image, and D_E is equal 3.

2.2 Samples. A pair of samples, one carbonate (G3) and one shaly-sandstone (ES3-1), was used in this study. The samples were selected from a group of four sandstones and four carbonates from two different reservoirs. The selection criterion was based on a consideration that the pair of carbonate and shaly-sandstone samples were comparable in terms of texture and porosity.

The shaly-sandstone sample which is moderately sorted, has subangular to angular grains with relatively poor to moderately developed primary and secondary porosities (Fig. 1(*b*)). The porosity measured by injecting helium into the core sample is 16.01%. Dissolved silicate and lithic grains contribute significantly to secondary porosity, whereas microporosity is present in carbonate and clay cement as well. On the other side, the carbonate sample is a grainstone (Fig. 1(*a*)) with sub-rounded to sun subangular grains, which is a nearly similar texture to the shaly-sandstone sample. The helium porosity of the carbonate sample

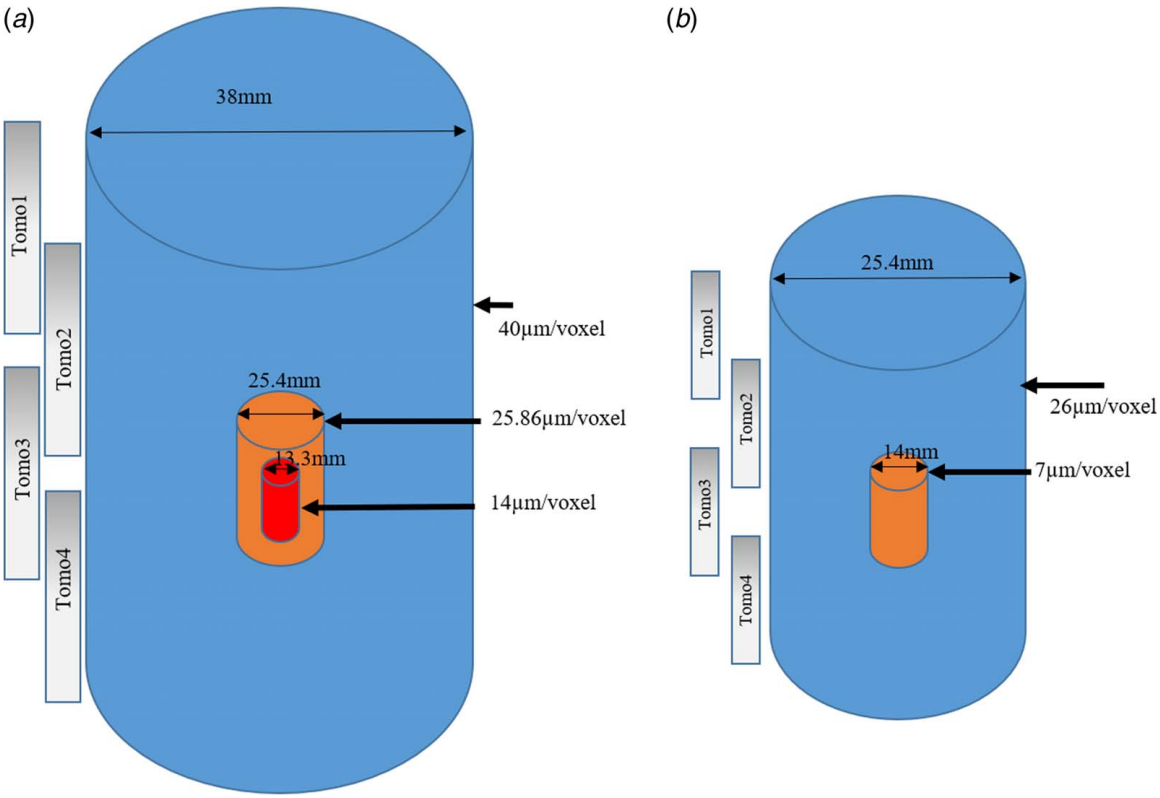

Fig. 2 Diagram showing the low-resolution imaging scheme: (*a*) imaging scheme for the carbonate sample (G3) and (*b*) imaging scheme for the shaly-sandstone sample (ES3-1). Note: first full plug was imaged in four separate tomograms (tomo1, tomo2, tomo3, and tomo4), then these tomos were stitched together to make one image.

is 15.3%, which is also very near to shaly-sandstone sample porosity. We denoted the shaly-sandstone sample as "ES3-1" and the carbonate sample as "G3."

Core plugs of 38 mm and 25.4 mm diameter from the carbonate and the shaly-sandstone sample, respectively, were initially used for low-resolution micro-CT imaging. Further, a 5 mm diameter sub-plug and a trim were drilled from the 25.4 mm and 38 mm core plugs, respectively (Figs. 2(*a*) and 2(*b*)), and used for high-resolution imaging in both samples. A larger sample size was chosen for carbonate rock keeping in view that it has larger upper limits of pore sizes.

2.3 Methods. The ability to resolve microstructures (resolution) in micro-CT is inversely proportional to sample size (diameter). It is quite necessary to know about sample microstructure (pore and grain size) to select a plug diameter to get required results before CT scanning. Before acquiring any image, we looked at the thin sections of the samples in an optical microscope to get a preliminary description and to compare the selected samples Then, CT imaging was performed in a X-ray micro-scanner (Zeiss Xradia versa 520, available in the Rock Physics Lab of ADNOC Research and Innovation Center—ADRIC). This equipment can provide 3D images approaching a maximum resolution of 0.5 μm/voxel for small samples (i.e., samples with a diameter of around 1 mm), depending on the sample characteristics. In addition, SEM images were acquired in a Philips-FEI Quanta 200 microscope available at Petroleum Geoscience Department in Khalifa University, Abu Dhabi. SEM can provide 2D images reaching a maximum resolution upto a nanometer [20]. An integrated imaging workflow, described in Secs. 2.4 and 2.5, was used to image the rock samples at multiscale and multiresolution, in both SEM and micro-CT to study the effects of scale and resolution. Multiscale here refers to imaging the rock at different plug sizes (i.e., 38 mm, 25.4 mm, and 5 mm), while multiresolution refers to imaging same plug at different resolutions using zooming.

2.4 Micro-Computed Tomography Imaging. X-ray CT provides a nondestructive way to image rock samples that is an ideal tool to characterize the internal structure of a rock in three dimensions [31]. While the limitation of this CT technique is that only small samples can provide high spatial resolution, and therefore, often multiple scanned images will be needed in order to obtain representative volumes [32–34]. The elaborated procedure of CT imaging includes the acquisition of a large number of X-ray projections. Computationally intensive numerical algorithm reconstructs these projections into a 3D volume. A series of two-dimensional slices stack into a 3D image. Data are arranged in an array of pixels in the two-dimensional slice. A pixel in the third dimension makes it three-dimensional volume which is a voxel. This is, the distance between two consecutive slices is a voxel. CT imaging can be categorized into low-resolution tomography and high-resolution tomography. We call here low-resolution tomography to those in the range of 40–10 μm/voxel, and high-resolution tomography to those between 10 and 0.5 μm/voxel. The Zeiss Xradia versa 520 has an "optical zooming" feature, which was used for each original sample and subsamples to acquire multiple resolution images. Sample size imaged resolution and optical zooming summary are present in Table 1.

2.4.1 Low-Resolution Tomography. The carbonate core plug of 65.55 cm^3 that had 38 mm diameter was scanned at three low resolutions (40.1, 25.86, and 14 μm/voxel) with only one optical zoom (Fig. 2(*a*)) of 0.4×. The shaly-sandstone core plug of 21.64 cm^3 that had of 25.4 mm diameter was scanned at two low resolutions (26 and 7 μm/voxel resolution) with only one optical zoom (Fig. 2(*b*)) of 0.4×. These core plugs of 38 and 25.4 mm diameter were imaged in four separate tomograms (Figs. 2(*a*) and 2(*b*)) with 60% overlap, and the overlap was used to stitch these tomograms together. In addition, single tomograms for the digital subsamples were acquired with optical zooming by selecting them in the center of the core plugs (Figs. 2(*a*) and 2(*b*)).

2.4.2 High-Resolution Tomography. Capturing pore structures approaching the scale of 1 μm or less was achieved using 5 mm diameter sub-plug extracted from 25.4 mm plug (Fig. 3(*a*)) from shaly-sandstone and trims from carbonate with high-resolution tomography. 5 mm diameter trim from the carbonate sample was imaged at 4 μm/voxel and 2.01 μm/voxel using the optical zoom of 4× and 0.4×, respectively (Fig. 4(*a*)). While 5 mm sub-sample from the sandstone was imaged at 5 μm/voxel (field of view (FOV): 5 mm), 2.5 μm/voxel (5 mm full plug), and 1.86 μm/voxel resolution using optical zooming of 4×, 14×, and 10×, respectively (Fig. 4(*b*)).

2.5 Scanning Electron Microscope Imaging. The SEM microscope was used to capture the microporosity in the studied samples. The term microporosity in this paper corresponds to the porosity that lies below the resolution of the micro-CT images, which is 0.5 μm/(voxel or pixel). SEM is a traditional high-resolution 2D imaging technique which can acquire images with submicron resolution. We used trimmed tops of the of 25.4 and 38 mm plugs from both samples to make thin sections. These trims were mounted on a standard glass plate with epoxy and polished very finely (Fig. 3(*b*)). The surface of the thin sections was coated with gold and platinum to avoid the electron charging

Table 1 Summary of image size, optical zooming, and resolution used for each sample in the micro-CT and SEM imaging

Image	Sample	Diameter (mm)	Resolution (μm/(voxel or pixel))		Optical zooming/ magnification	Volume (voxel)
Micro-CT	ES3-1	25.4	Low	26	0.4×	500 × 500 × 500
				7	0.4×	1000 × 1000 × 1000
		5	High	5	4×	500 × 500 × 500
				2.5	14×	1000 × 1000 × 1000
				1.86	10×	500 × 500 × 500
	G3	38	Low	40.16	0.4×	500 × 500 × 500
				25.86	0.4×	500 × 500 × 500
				14	0.4×	500 × 500 × 500
		5	High	4	4×	500 × 500 × 500
				2.01	10×	500 × 500 × 500
SEM	ES3-1			1.69	70×	7155 × 7155
				0.12	1000×	9536 × 9536
	G3			2.7	62×	6784 × 6784
				0.67	120×	11,808 × 11,808
				0.12	1000×	8016 × 8016

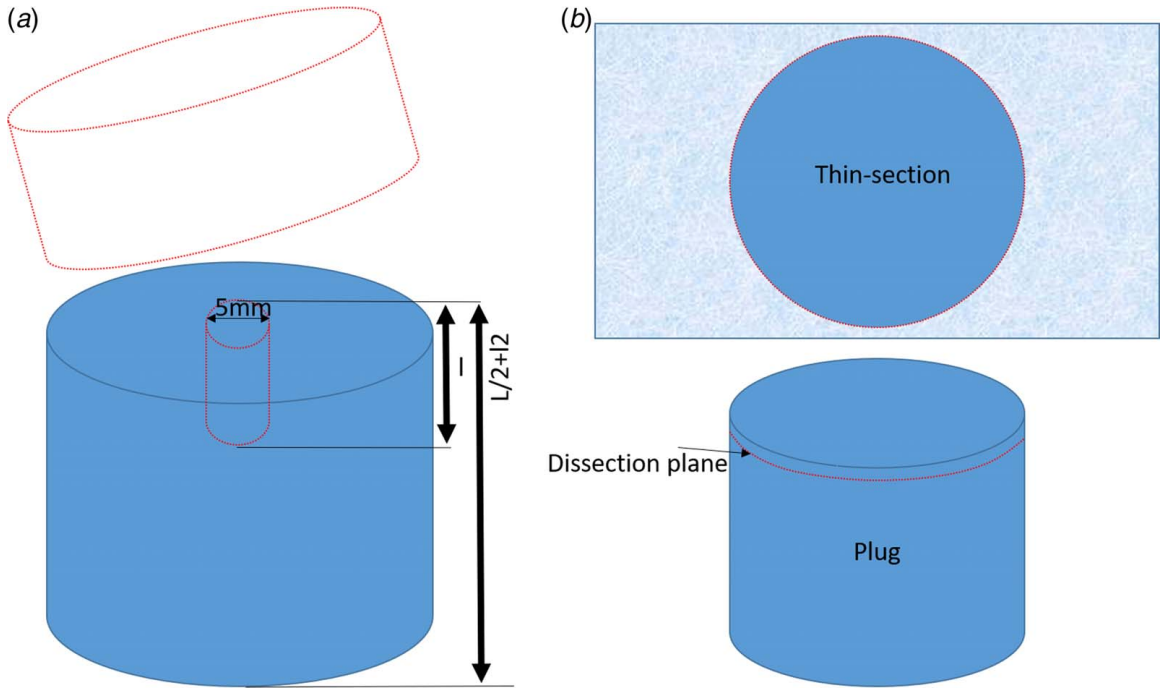

Fig. 3 An illustrative diagrame showing method for the extraction of sub-plugs and thin section chips: (*a*) sub-plug from shaly-sandstone plug and (*b*) SEM thin section from both carbonate and sandstone plugs

effect in SEM images. A preliminary study was made to infer optimal magnification for two scales of imaging (full thin section and selected subregion). Then, a series of images were acquired under the same magnification and stitched together to get a mosaic image. For the carbonate sample, 82, 25, and 25 images were acquired and stitched together for each three magnifications 62×, 120×, and 1000×, respectively. For the shaly-sandstone sample, 96 and 46 images were acquired and stitched together for 70× and 1000×, respectively (Table 1).

2.6 Image Processing. In the case of micro-CT images, the attenuation of X-rays usually produces a beam hardening artifact, which directly affects visual inspection and automated segmentation of micro-CT images [31]. The bean hardening artifact is termed as false density gradients which appear as streaks between highly attenuating structures. Most of these features appear in the outer regions of the sample resulting in some brighter outer rims. The strength of this artifact is sensitive to many factors, including the shape and geometry of the sample, energy spectrum used for

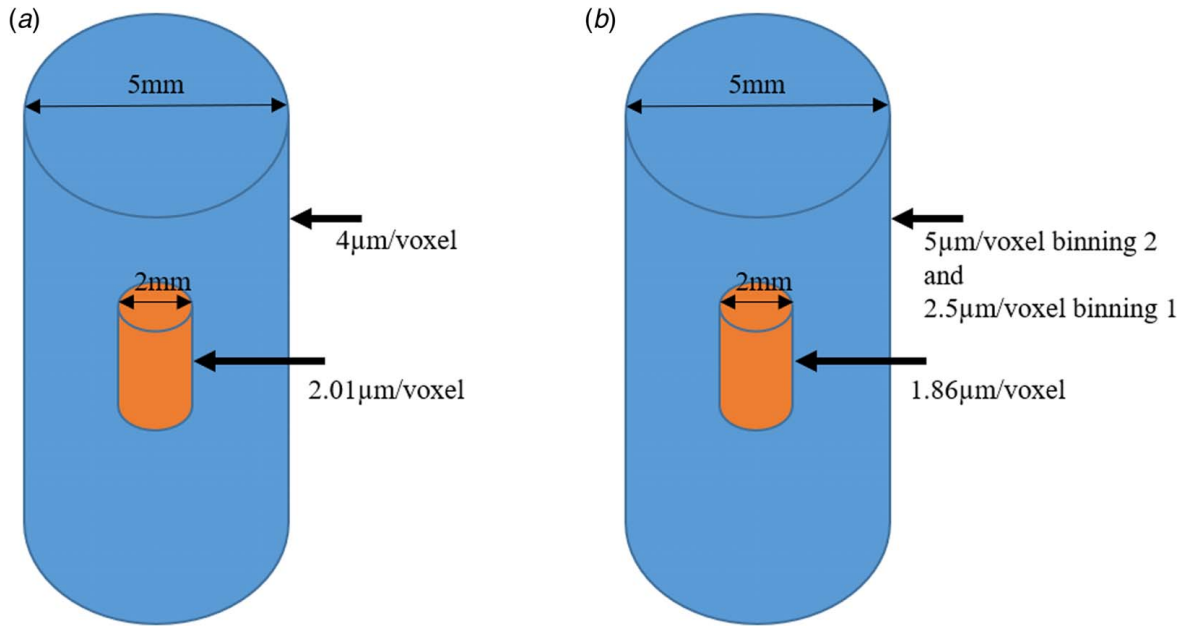

Fig. 4 Diagram illustrates the high-resolution imaging scheme: (*a*) imaging scheme for the carbonate sample (G3) and (*b*) imaging scheme for the shaly-sandstone sample (ES3-1). Note: the shape of the carbonate trim sample was irregular, so we used optical zoom to get the cylindrical image.

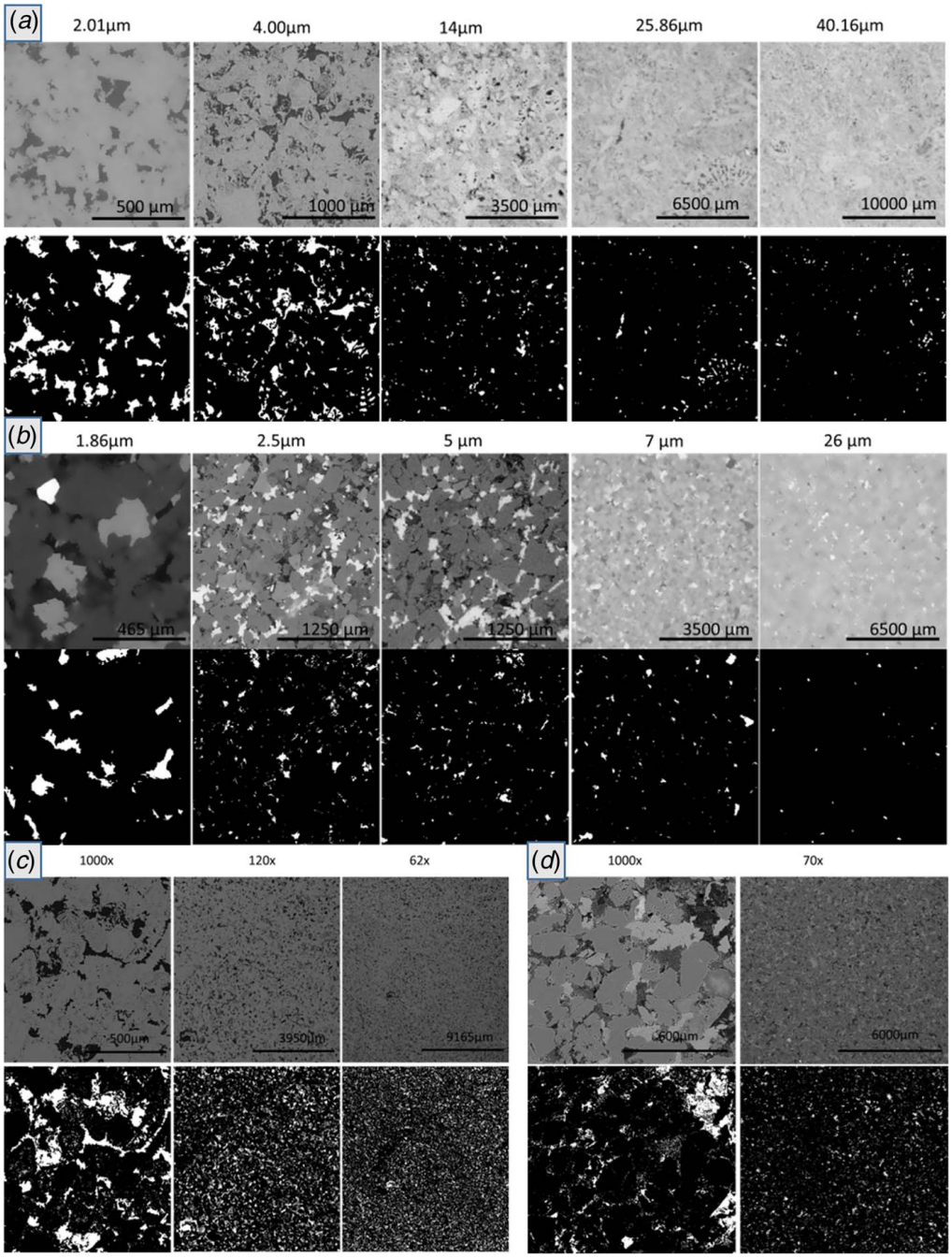

Fig. 5 Original (in grayscale) and segmented images (black and white) from micro-CT and SEM: (*a*) 2D slices from shaly-sandstone CT tomogram at different resolutions (26, 7, 5, 2.5, and 1.86 μm/voxel); (*b*) 2D slices from carbonate CT tomogram at different resolutions (40.16, 25.86, 14, 4, and 2.01 μm/voxel); (*c*) SEM images from the carbonate sample at different magnifications (62×, 120×, and 1000×); (*d*) SEM images from sandstone sample at different magnifications (70× and 1000×). The gray colors in the original images correspond to different grades of high-density material, and the white color is the lowest density material, such as pores. The black color in the segmented images corresponds to the solid part, and the white color corresponds to the pores.

source X-ray, and density distribution within the sample. To correct and avoid this artifact, the edges of the samples were eliminated.

Except for the above-explained artifact correction, the image processing for both, SEM and micro-CT images, was done in the same consisting way. Both SEM and micro-CT images were cropped into maximum possible squares and cubes, respectively. The cropped images were filtered using a non-local mean filter to reduce noise and enhance pore space segmentation. Then, the images were manually segmented by selecting pore-solid boundary on image gray-level histograms. Segmented images were thoroughly studied and compared with the original image to check segmentation quality (Fig. 5). Pore space threshold for each segmented image is present in Table 2.

2.7 Calculation of Fractal Dimension. Fractal count plugin in the open access IMAGEJ software is based on an algorithm developed by Chen et al. [35] to calculate the fractal dimension of pore space, which is used in this study. Beside conventional box-counting software, this software has two advantages. First, it provides an improved way in a sense that boxes are not locked to a

Table 2 Summary of the segmentation threshold for each image used in this study

Image	Sample	Resolution (μm)	Pore threshold
Micro-CT	ES3	26	149
		7	141
		5	37
		2.5	57
		1.86	37
	G3	40.16	149
		25.86	136
		14	114
		4	76
		2.01	128
SEM	ES3-1	1.69	43
		0.12	50
	G3	2.7	70
		0.67	63
		0.12	60

Note: 16-bit images were converted to 8 bit before segmentation, and a total number of gray values is 255 for each image.

grid in the z-direction, and they moved up and down to find the lowest number of boxes needed for the calculation. Second, this software supports both, 3D and 2D, binary images for calculations in the same way.

3 Results and Discussion

3.1 Image Porosity. Image porosity calculated by Eq. (4) for the 3D CT scan images of samples G3 and ES3-1 results in a function of e image resolution. As the image resolution gets higher (i.e., the values decrease), a greater number of smaller pores become resolved, and consequently the image porosity increases (Fig. 6(*a*)). This point is also evident from a visual inspection of the CT scan segmented images at different resolutions in the bottom rows of Figs. 5(*a*) and 5(*b*). In fact, G3 and ES3-1 samples show that the image porosity from CT scans versus resolution follows an exponential law (Fig. 6(*a*)). On the other hand, there is not a clear relationship for the 2D SEM images (Fig. 6(*b*)) because of the limited number of different resolutions.

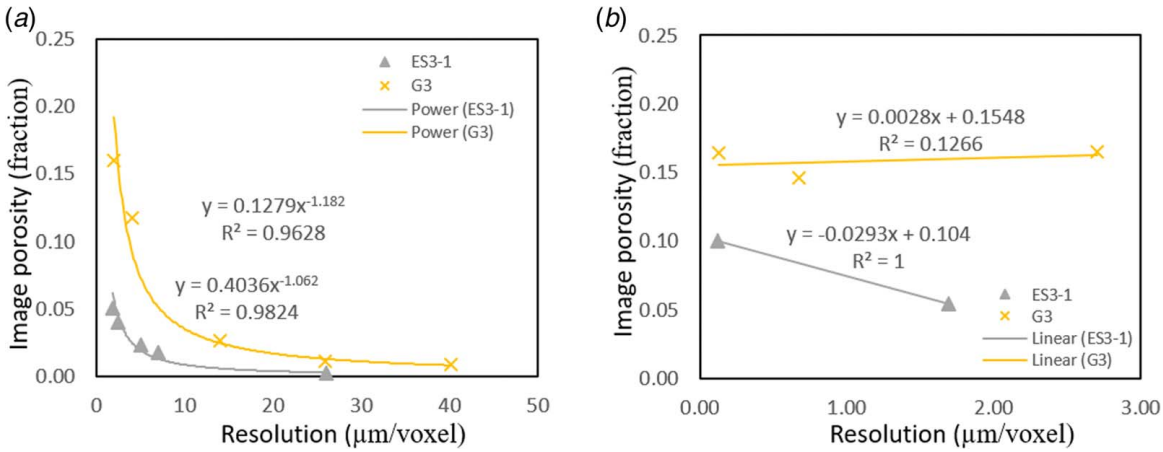

Fig. 6 Graphs showing the image porosity versus image resolution from the (*a*) micro-CT images and (*b*) SEM images

Table 3 Parameters derived from micro-CT and SEM image analysis

Image	Sample	Resolution (μm/(voxel or pixel))	Average pore radius (μm)	e' (for average)	Median pore radius (μm)	e' (for median)	Fractal dimension (D0)	Fractal-scaling porosity for average pore size (fraction)	Fractal-scaling porosity for median pore size (fraction)	Image porosity (fraction)	Core porosity (fraction)
Micro-CT	ES3-1	26	38.07	0.003	156	0.012	1.81	0.001	0.005	0.002	0.160
		7	23.15	0.007	105	0.015	2.40	0.050	0.082	0.018	
		5	9.68	0.004	50	0.020	2.38	0.032	0.088	0.023	
		2.5	8.14	0.007	60	0.024	2.63	0.153	0.248	0.040	
		1.86	8.15	0.009	29.76	0.032	2.52	0.103	0.191	0.050	
	G3	40.16	159.80	0.008	562.24	0.028	2.20	0.021	0.058	0.008	0.153
		25.86	76.72	0.006	232.74	0.018	2.26	0.023	0.051	0.011	
		14	29.64	0.004	154	0.022	2.54	0.082	0.174	0.026	
		4	11.72	0.006	84	0.042	2.69	0.199	0.370	0.118	
		2.01	12.32	0.012	46.02	0.046	2.60	0.174	0.293	0.160	
SEM	ES3-1	1.69	17.88	0.001	50.7	0.004	1.66	0.111	0.158	0.054	0.16
		0.12	7.24	0.006	14.384	0.012	1.60	0.132	0.174	0.100	
	G3	2.70	32.4	0.002	121.5	0.007	1.85	0.385	0.470	0.165	0.15
		0.67	25.98	0.003	91.79	0.012	1.76	0.248	0.338	0.146	
		0.12	17.64	0.018	26.88	0.027	1.67	0.261	0.300	0.164	

Note: The parameters include average pore size, median pore size, fractal dimension, fractal-scaling porosity, image porosity, and core porosity.

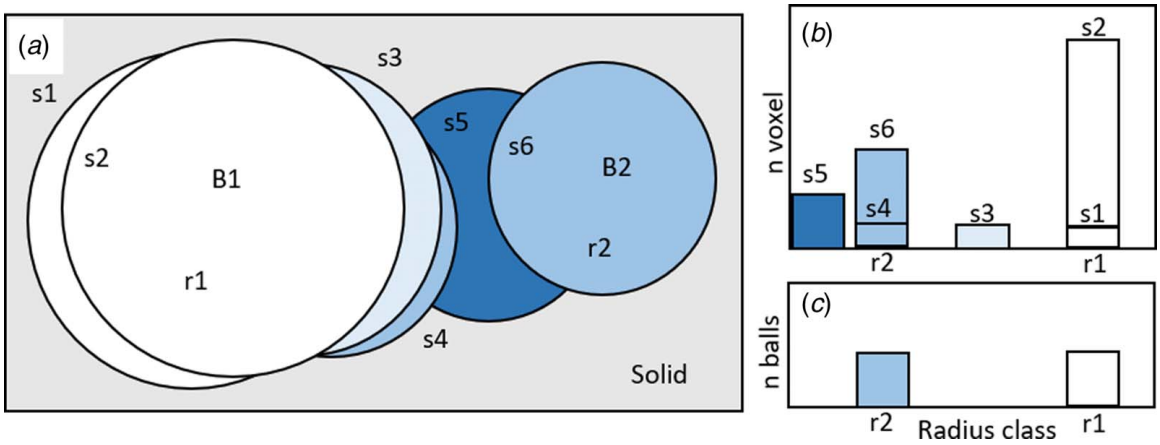

Fig. 7 Illustration of the aperture map computation. (*a*) For every voxel of the pore phase, the radius of the maximal balls is calculated that enclose the pore voxel at that location. (*b*) Aperture map distribution from every voxel of the pore phase. (c) This histogram reports the number of totally included balls (here only two B1 and B2) that have been found in the pore phase. Modified from Vicente et al. [37].

The calculated image porosity in 2D and 3D is different in the shaly-sandstone and carbonate samples. In the carbonate sample, the image porosity at the highest studied resolutions (2.01 μm/voxel in the CT and 0.12 μm/pixel in the SEM) is 95.6% of the core porosity (Table 3). Whereas in the sandstone sample, the image porosity at the highest studied resolutions (1.86 μm/voxel in the CT and 0.12 μm/pixel in the SEM) is lower (31% and 62.5%, respectively) than the measured core porosity (Table 3). These results indicate that the micro-CT scan and SEM images failed to resolve fully the pore space in the shaly-sandstone sample.

3.2 Pore Size Distribution. Pore size distribution is defined as the pore and throat size and distribution, and their connectivity as well as the spatial distributions of all these properties [36]. IMORPH, an open-source software, was used to find the PSD of the 3D and 2D images. This software works on the binary image where it calculates the radius of maximal ball-size for every voxel in the pore phase (Fig. 7(*a*)). This radius is called aperture radius. The mean value of the aperture radius distribution is used to give a first approximation of the phase diameter [37]. The distribution of the maximal included balls gives information on how pores are distributed in the media (Figs. 7(*b*) and 7(*c*)). The same method is used to get PSD from SEM images and the CT scan images. As the software only accepts 3D images, for the SEM images in 2D, the third (z) dimension was used as null. It is worth mentioning here that the pore volume divided by the total volume found by this method is equal to the image porosity found in Sec. 3.1, which is an evidence of the consistency of this method. Pore extracted with this method was assumed as the natural model (scale-free), that have an essentially fractal topology [38].

The resulting pore size (pore radius) is plotted against its corresponding percent volume for micro-CT and SEM images in Fig. 8. Both samples, G3 and ES3-1, at all resolutions show log normal distribution of pore radius. Basically, the samples used here are very similar in terms of their granular texture. However, the main difference lies in the pore size distribution, where the carbonate sample shows higher upper pore size limits (522 μm in CT and 118 μm in SEM) than the sandstone (130 μm is CT and 49 μm in SEM). Both, SEM and CT PSD display that biggest population of pore lies over 10 μm in the carbonate sample (Figs. 8(*a*) and 8(*c*)) while in sandstone biggest population lies below 10 μm (Figs. 8(*b*) and 8(*d*)). However, the pore size distribution for both, carbonate and sandstone sample, at the highest resolution (0.12 μm/pixel) in the SEM images revealed that a small pore population (Figs. 8(*d*) and 8(*e*)) exists below 1 μm size. Bigger pore size (termed as macroporosity) usually corresponds to intergranular pore in both studied samples. However, the pores that lie below 1 μm (microporosity) correspond to intercrystalline pore in the clay of the shaky-sandstone and in the micrite in the carbonate sample. We found that the resolved porosity in 2D and 3D images are a function of the resolution. As resolution improves, the upper limit of pore size and highest population peak also shifts toward higher resolutions. High-resolution imaging could not detect bigger pore properly in micro-CT due to the smaller (2 mm or less) field of view, which might not represent elementary volume. Therefore, it is a key necessity to integrate multiscale observation, including low, high-resolution tomography, and SEM imaging, to cover the whole pore spectrum.

The mode value from the PSD corresponds to the lower pore size limit as well as the voxel size (resolution) of the image in both samples in all images resolutions. This is because the tendency to detect and resolve the smallest feature in the digital image is as high as its voxel size. Arithmetic means, median, mode, and weighted average (Eq. (9)) lie very close to each other at higher resolution, whereas they separate apart at low resolutions (Figs. 9(*a*) and 9(*b*)). Here, the weighted average is the mean of the pore size weighted by volume occupancy. Usually, the arithmetic means and median pore size are the same at each resolution in the G3 sample because the pore radius data set is evenly spaced. However, in the ES3-1 sample, there are some exceptions, where the mean pore size lies lower than the median and very close to average pore size at 5 μm/voxel and 7 μm/voxel resolution (Fig. 9(*b*)). The resulting distribution curves are non-Gaussian with long tails that is why the weighted average and the median pore sizes are suitable here to represent the central tendency of pore spectrum

$$\text{weighted average} = \frac{\sum r_p \times V_p}{\sum V_p} \tag{9}$$

where r_p is the pore radius and v_p is the pore volume.

3.3 Fractal Dimension. The degree of irregularity of an object or set of objects defines its ability to fill a Euclidean space [10,36]. As the fractal dimension is a kind of measure of the irregularity of a self-similar object/set, it can be considered as a measure of the ability of that object/set to fill the space in which it resides [39,40]. As a matter of fact, the more irregular the self-similar object/set is, the more the Euclidian space is filled [41]. As the fractal dimension (D_O) approaches and gets closer to a Euclidean dimension (D_E), the more that the Euclidian space is filled. In the practical case of the pore space in a rock, the more that Do gets closer to D_E, the more that the pore space is filled with the

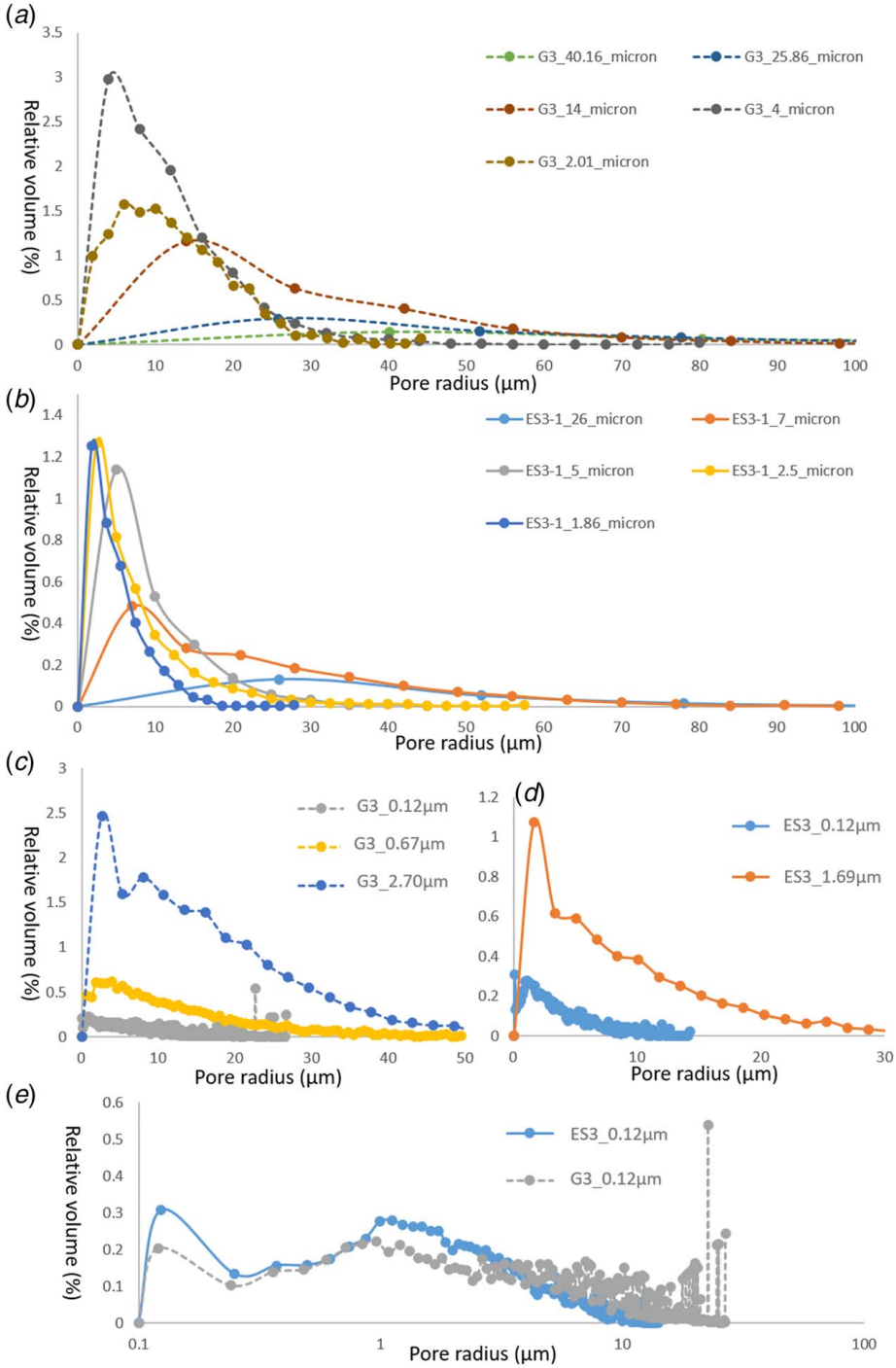

Fig. 8 Frequency curve showing PSD from sandstone and carbonate and sandstone images multiple resolution: (*a*) G3 carbonate CT, (*b*) sandstone ES3-1 CT, (*c*) G3 carbonate SEM, (*d*) ES3-1 sandstone SEM, and (e) ES3-1 and G3 PSD from 0.12 μm/pixel resolution image on the logarithmic scale

corresponding fractal. Cai and Yu [3] also calculated maximum pore size using fractal geometry based on porosity and permeability data, imbibition coefficient data. The fractal dimension method tested on sandstone micro-CT images shows a self-similar fractal range when excluding smaller pores [42].

In accordance with the imaging work flow, we calculated fractal dimension for each imaged resolution. In general, we found that the fractal dimension increases in the 3D CT scan images as image resolution and image porosity increase; but it decreases in the 2D SEM as image resolution and image porosity increase. A close look of the image resolutions of the CT scan images data (Table 3) shows that the fractal dimension increases from its lowest value at the lowest resolution (26 μm/voxel and 40.16 μm/voxel, for ES3-1 and G3, respectively) and reaches its highest value at the second highest image resolution (2.5 μm/voxel and 4 μm/voxel, for ES3-1 and G3, respectively), and decreases at the highest image resolution (1.86 μm/voxel and 2.01 μm/voxel, for ES3-1 and G3, respectively). In our opinion, this change in the fractal dimension trend marks a switch in the fractal scale. In addition, the fractal dimension decreases with the image resolution in the SEM images following

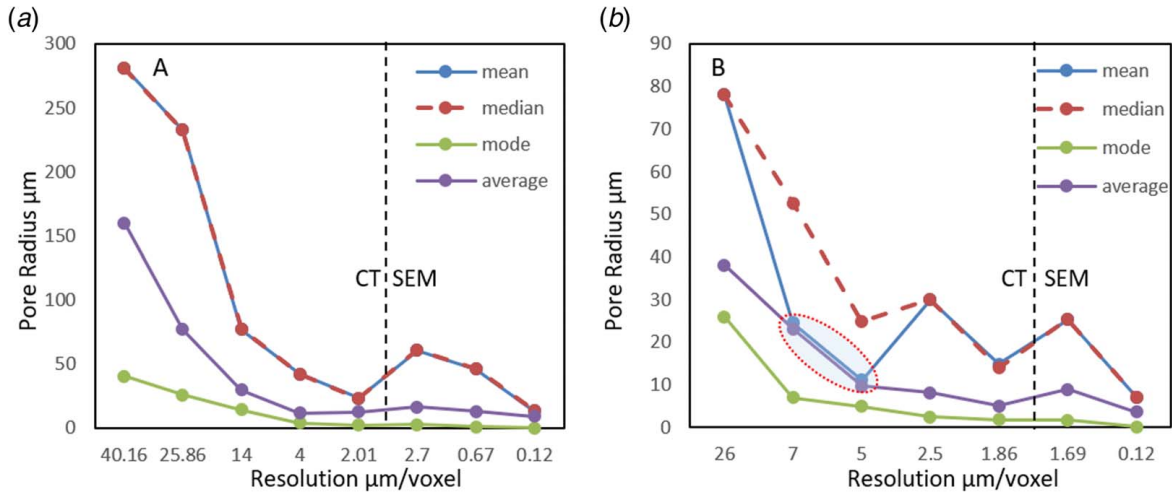

Fig. 9 The arithmetic mean, median, mode, and the weighted average pore radius calculated from PSD at different resolutions: (*a*) carbonate (G3) and (*b*) sandstone (ES3-1)

the same trend for resolutions higher than 1.86 μm/voxel and 2.01 μm/voxel, for ES3-1 and G3, respectively.

As we discussed before, the PSDs in the carbonate and shaly-sandstone sample are quite different, where the micro-CT scan images were unable to capture the full pore spectrum in the shaly-sandstone. This difference in PSD yielded different image porosity versus fractal dimension trends among both samples (Fig. 10(*a*)), where the shaly-sandstone observes steeper trends than the carbonate sample.

3.4 Fractal-Scaling Porosity. Fractal objects follow scaling laws and are self-similar, i.e., independent of the scale of

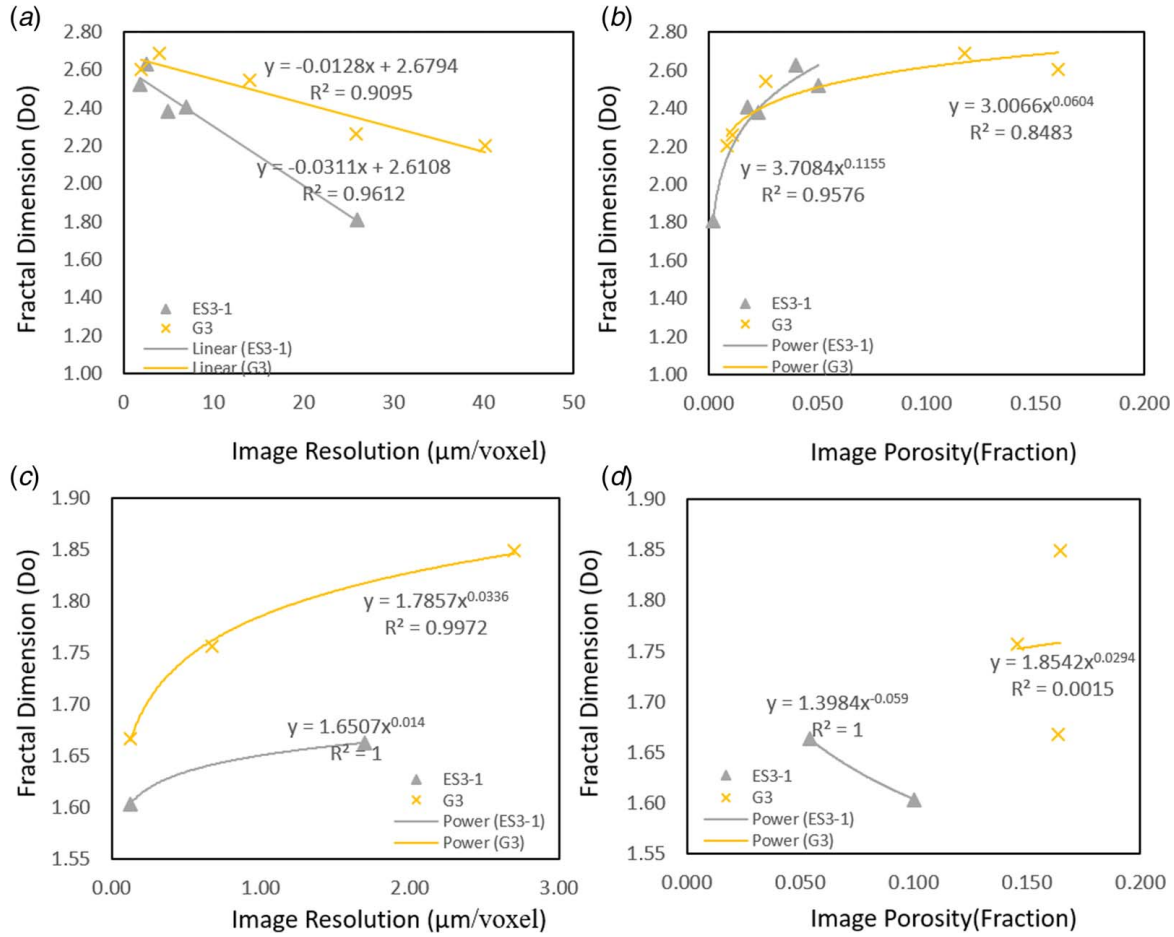

Fig. 10 Point scatter graph showing the relation between fractal dimension and image resolution and image porosity: (*a*) fractal dimension versus image resolution from micro-CT, (*b*) fractal dimension versus image porosity from micro-CT, (*c*) fractal dimension versus image resolution from SEM, and (*d*) fractal dimension versus image porosity from SEM

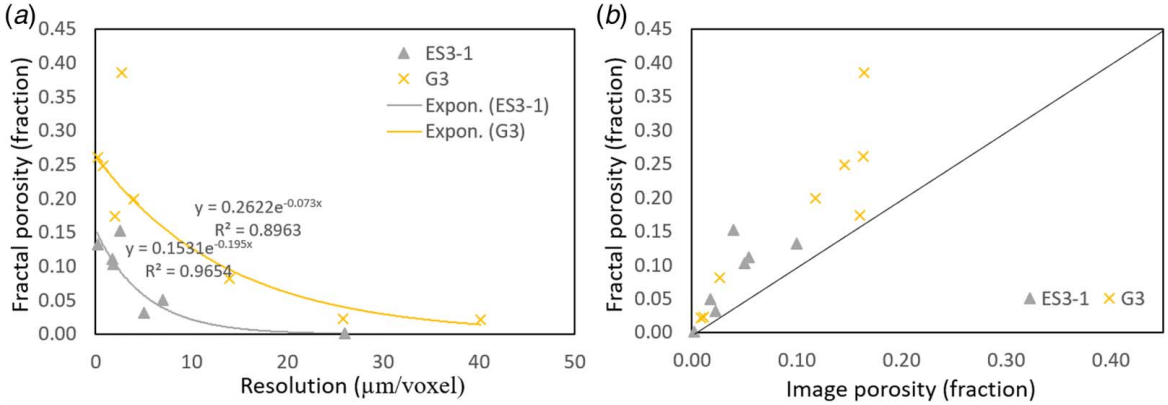

Fig. 11 (*a*) Point scatter plot showing the exponential relation between image resolution and fractal-scaling porosity and (*b*) scatter of data points showing calculation difference between fractal image porosity. The black line marks perfect fit where both axes have the same values.

measurement [43]. This unique property of fractal objects is utilized by Vega and Jouini [14] to develop an equation to estimate the fractal-scaling porosity. This equation was deducted under the approximation that all of the pores have the same size. To evaluate the potential effect of this approximation, they used the minimum, maximum, and average pore size to calculate the fractal-scaling porosity. From the pore size analysis study, it is evident that median and weighted average pore size are suitable candidates to represent the central tendency of pore spectrum. Therefore, we used the median and the weighted average pore size in the equation to calculate the fractal-scaling porosity. The use of these two statistics show quite different results, in overall, the weighted average pore size gives good estimates (Table 3), but in the shaly-sandstone SEM images, median pore size produces better estimated than the average (Table 3). In addition, our results show that increasing the image resolution, the fractal-scaling porosity also increases in both samples (Fig. 11(*a*)). The trend line is in the agreement with the trend found in the resolution versus image porosity in the figure. The image porosity versus fractal-scaling porosity plot shows that the fractal-scaling porosity is always higher than the image porosity, only a few points give almost a perfect match (Fig. 11(*b*)). Those points coincide with the highest value of Do for ES3-1 and the highest resolution for G3 in the CT scan images. The calculated fractal-scaling porosity in the SEM images of the shaly-sandstone sample provides a very good match with the core plug porosity, for both average and median pore size: while in the carbonate sample, the estimation is always overestimated (Table 4).

In the carbonate sample in general, the fractal-scaling porosity seems to give a better result than the image porosity at the lowest resolution of 40 μm/voxel and an acceptable relative error, less than 30%, at the highest CT resolutions of 4 and 2.01 μm/voxel. On the other hand, for the SEM images of the shaly-sandstone sample, the estimation of image porosity does a better job than the fractal-scaling porosity in the carbonate sample.

Table 4 Showing error in image and fractal-scaling porosity calculated relative to core porosity

Image	Sample	Resolution (μm/(voxel or pixel))	Relative error (image porosity)	Relative error (fractal-scaling porosity)
Micro-CT	ES3-1	26	99	99
		7	89	69
		5	86	80
		2.5	75	5
		1.86	68	36
	G3	40.16	94	86
		25.86	93	85
		14	83	46
		4	23	30
		2.01	5	14
SEM	ES3-1	1.69	66	31
		0.12	37	17
	G3	2.70	8	60
		0.67	4	39
		0.12	7	42

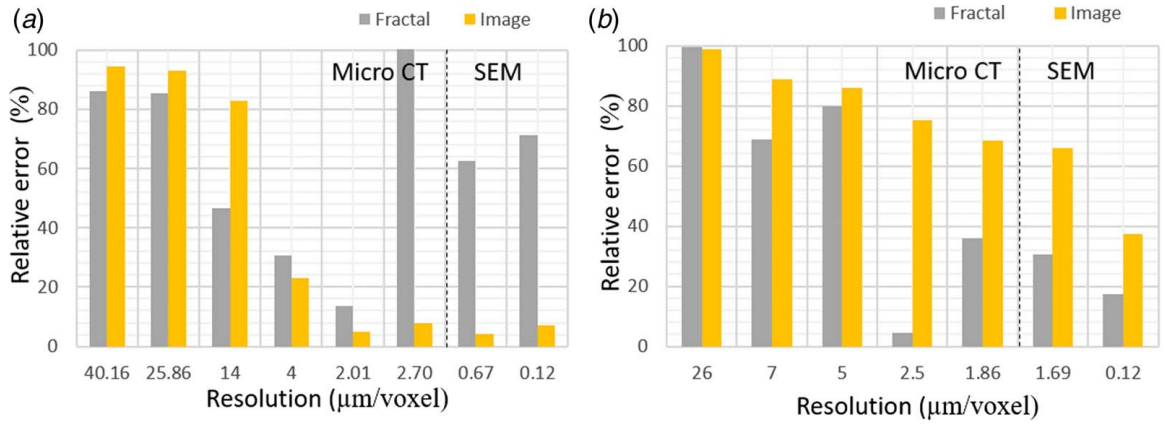

Fig. 12 Bar graph showing a relative error for calculated fractal and image porosity against image resolution: (*a*) carbonate sample G3 and (*b*) sandstone sample ES3-1

In the case of 2D SEM images, the predictions are better in the shaly-sandstone sample where there is a short tail in the pore size distributions. This is similar to what Vega and Jouini [14] found before for carbonates in 2D images, where the pore size distribution was simple and unimodal, and the predictions were better. Whereas, in this study, the carbonate sample, although has a unimodal PSD but with a long tail. Therefore, the fractal-scaling porosity predictions are less good.

In CT images, the fractal-scaling porosity seems to give a better estimate than image porosity at all resolutions, while the SEM of carbonate does not provide good results. This may be due to the fact that the fractal behavior in the shaly-sandstone sample is captured at all measured scales, while SEM failed to capture the fractal behavior in the carbonate sample. Therefore, fractal-scaling porosity seems to be more useful for the studied shaly-sandstone sample than for the carbonate sample. The best estimation is given at 2.5 μm/voxel in the CT scan image of the carbonate sample with a relative error of only 5%, followed by the estimations of the shaly-sandstone sample at the SEM higher resolutions of 1.69 and 0.12 μm/pixel, where the relative error is 31% and 17%, respectively (Fig. 12(*b*)). The equation for relative error that we use is given by

$$\text{Relative error} = \left(\frac{\text{core porosity} - \text{image or fractal porosity}}{\text{core porosity}}\right) \times 100 \tag{10}$$

Then, the results in the SEM images here suggest that they are an alternative inexpensive way to calculate the fractal-scaling porosity in the shaly-sandstone sample where it was able to capture the full fractal character. On the other hand, the relatively poorer estimation of the fractal-scaling porosity in the carbonate SEM images might be due to the 2D SEM images did not capture of the full fractal of the pore space in the carbonate rock.

4 Conclusion

In this study, we took digital images of a carbonate and a shaly-sandstone sample with micro-CT scans and SEM techniques at multiple scales and resolutions. The systematic multiscale imaging plan was used to capture the fractal behavior of pore space. The following conclusions can be drawn:

- Pore size distribution seems to play an important effect on the application of the fractal-scaling porosity. Our results suggest for the SEM images that to get a good prediction from the fractal-scaling porosity equation, the PSD needs to comply with: (1) unimodal distribution, and (2) the PSD curve tail should be a short. As a matter of fact, this equation can be very useful to predict porosity at higher resolutions from cuttings, if the PSD curve shows short tail in a unimodal pore size distribution.
- In the case of 3D micro-CT scan images: There is no clear correlation between the PSD curve shape and the porosity predictions using the fractal-scaling porosity equation. Hence, more studies are needed for the prediction of the fractal-scaling porosity for 3D images. So, we suggest for future work to include explicitly the pore size distribution in the equation instead of using a singular pore size.
- The fractal-scaling porosity calculated from the *Vegas* equation delivered interesting results. This equation is predicting a good estimation of the porosity even in those cases where full pore space cannot be captured by conventional imaging techniques. However, care must be done while applying this equation because the fractal character can be present at a specific scale that might not be at the scale of interest. That is why this equation is only valid when the upper limit of self-similarity is equal to or greater than the image size, and the lower limit is lesser than or equal to the image resolution. The results can vary from rock to rock, that is why sensible multiscale imaging methodology should be designed to capture important parameters such as PSD which might be affected by the fractal and multifractal nature of the rock.
- In this study we used multiscale imaging methodology to capture full pore spectrum and fractal behavior of pore space. A resolution of 2.5 μm/voxel in the shaly-sandstone sample and 2.01 μm/voxel in the carbonate sample provided the best match with the core plug porosity in the CT scan images. SEM images from the shaly-sandstone also provided a relatively good match with the core plug porosity. Comprehensive imaging details and the comparison of pore size distribution and fractal behavior of pore space at different scales provide a platform for future fractal studies to select the imaging scale and technique in these kinds of rock.

Results showed a great potential to scale porosity by this equation, but this study is based on only in two samples. Extensive learning is needed to validate and optimize the fractal-scaling porosity calculation and methodology. Future studies can include different rock types and a bigger number of samples. Moreover, the effect of pore size approximation can be reduced or eliminated by using pore size distribution function rather than single or average pore size.

Acknowledgment

The work has been financially supported by the "National Science and Technology, P.R. China" Project (Special Grant No. 2016ZX05027004-002, 41672129) and ADNOC project OSC 13003. Special thanks to Geosciences Institute of the Shengli Oilfield, SinoPec and ADNOC for providing well cores for this study.

Conflict of Interest

There are no conflicts of interest.

References

[1] Mandelbrot, B. B., 1982, *The Fractal Geometry of Nature*, Revised ed., W. H. Freeman and Company, San Francisco.
[2] Katz, A. J., and Thompson, A. H., 1985, "Fractal Sandstone Pores: Implications for Conductivity and Pore Formation," Phys. Rev. Lett., **54**(12), pp. 1325–1328.
[3] Cai, J., and Yu, B., 2011, "A Discussion of the Effect of Tortuosity on the Capillary Imbibition in Porous Media," Transp. Porous Media, **89**(2), pp. 251–263.
[4] Wang, S., and Yu, B., 2011, "Study of the Effect of Capillary Pressure on the Permeability of Porous Media Embedded With a Fractal-Like Tree Network," Int. J. Multiph. Flow, **37**(5), pp. 507–513.
[5] Harte, D., 2001, *Multifractals*, Chapman & Hall, London.
[6] Falconer, K. J., and Lammering, B., 2003, "Fractal Properties of Generalized Sierpiński Triangles," Fractals, **6**(1), pp. 31–41.
[7] Wong, P. Z., Howard, J., and Lin, J. S., 1986, "Surface Roughening and the Fractal Nature of Rocks," Phys. Rev. Lett., **57**(5), pp. 637–640.
[8] Krohn, C. E., 1988, "Fractal Measurements of Sandstones, Shales, and Carbonates," J. Geophys. Res., **93**(B4), p. 3297.
[9] Padhy, G. S., Lemaire, C., Amirtharaj, E. S., and Ioannidis, M. A., 2007, "Pore Size Distribution in Multiscale Porous Media as Revealed by DDIF-NMR, Mercury Porosimetry and Statistical Image Analysis," Colloids Surf., A, **300**(1–2), pp. 222–234.
[10] Xie, S., Cheng, Q., Ling, Q., Li, B., Bao, Z., and Fan, P., 2010, "Fractal and Multifractal Analysis of Carbonate Pore-Scale Digital Images of Petroleum Reservoirs," Mar. Pet. Geol., **27**(2), pp. 476–485.
[11] Zhang, F., Zhou, H., and Z, Y., 2010, "3D Reconstruction of Rock Cracks CT Image Fractal Damage Study," *Information Technology in Geo-Engineering*, D. G. Toll, ed., IOS Press, Amsterdam, The Netherlands, pp. 157–166.
[12] Jouini, M. S., Vega, S., and Mokhtar, E. A., 2011, "Multiscale Characterization of Pore Spaces Using Multifractals Analysis of Scanning Electronic Microscopy Images of Carbonates," Nonlinear Proc. Geoph., **18**(6), pp. 941–953.
[13] Zhang, Z., and Weller, A., 2014, "Fractal Dimension of Pore-Space Geometry of an Eocene Sandstone Formation," Geophys., **79**(6), pp. D377–D387.
[14] Vega, S., and Jouini, M. S., 2015, "2D Multifractal Analysis and Porosity Scaling Estimation in Lower Cretaceous Carbonates," Geophys., **80**(6), pp. D575–D586.
[15] Liu, Y., Liu, Y., Sun, L. U., and Liu, J., 2016, "Multiscale Fractal Characterization of Hierarchical Heterogeneity in Sandstone Reservoirs," Fractals, **24**(03), p. 1650032.
[16] Zhang, S., Xian, X., Zhou, J., Liu, G., Guo, Y., Zhao, Y., and Lu, Z., 2018, "Experimental Study of the Pore Structure Characterization in Shale With Different Particle Size," ASME J. Energy Resour. Technol., **140**(5), p. 054502.

[17] Davis, H. T., 1989, "On the Fractal Character of the Porosity of Natural Sandstone," EPL, **8**(7), pp. 629–632.
[18] Angulo, R. F., Alvarado, V., and Gonzalez, H., 1992, "Fractal Dimensions From Mercury Intrusion Capillary Tests," SPE Latin America Petroleum Engineering Conference, Caracas, Venezuela, Mar. 8–11, pp. 255–263.
[19] Li, K., 2004, "Generalized Capillary Pressure and Relative Permeability Model Inferred From Fractal Characterization of Porous Media," SPE Annual Technical Conference and Exhibition, Houston, TX, Sept. 26–29.
[20] Zhao, X., Yang, Z., Lin, W., Xiong, S., Luo, Y., Wang, Z., Chen, T., Xia, D., and Wu, Z., 2019, "Study on Pore Structures of Tight Sandstone Reservoirs Based on Nitrogen Adsorption, High-Pressure Mercury Intrusion, and Rate-Controlled Mercury Intrusion," ASME J. Energy Resour. Technol., **141**(11), p. 112903.
[21] Pape, H., Riepe, L., and Schopper, J. R., 1987, "Theory of Self-Similar Network Structures in Sedimentary and Igneous Rocks and Their Investigation With Microscopical and Physical Methods," J. Microsc., **148**(2), pp. 121–147.
[22] Stallmach, F., Vogt, C., Kärger, J., Helbig, K., and Jacobs, F., 2002, "Fractal Geometry of Surface Areas of Sand Grains Probed by Pulsed Field Gradient NMR," Phys. Rev. Lett., **88**(10), p. 105505.
[23] Zhang, P., Lu, S., Li, J., Chen, C., Xue, H., and Zhang, J., 2018, "Petrophysical Characterization of oil-Bearing Shales by Low-Field Nuclear Magnetic Resonance (NMR)," Mar. Pet. Geol., **89**(Part 3), pp. 775–785.
[24] Ren, X., Li, A., Memon, A., Fu, S., Wang, G., and He, B., 2019, "Experimental Simulation on Imbibition of the Residual Fracturing Fluid in Tight Sandstone Reservoirs," ASME J. Energy Resour. Technol., **141**(8), p. 082905.
[25] Krohn, C. E., and Thompson, A. H., 1986, "Fractal Sandstone Pores: Automated Measurements Using Scanning-Electron-Microscope Images," Phys. Rev. B, **33**(9), pp. 6366–6374.
[26] Krohn, C. E., 1988, "Sandstone Fractal and Euclidean Pore Volume Distributions," J. Geophys. Res., **93**(B4), p. 3286.
[27] Chen, X., Yao, G., Cai, J., Huang, Y., and Yuan, X., 2017, "Fractal and Multifractal Analysis of Different Hydraulic Flow Units Based on Micro-CT Images," J. Nat. Gas Sci. Eng., **48**, pp. 145–156.
[28] Thompson, A. H., Katz, A. J., and Krohn, C. E., 1987, "The Microgeometry and Transport Properties of Sedimentary Rock," Adv. Phys., **36**(5), pp. 625–694.
[29] Posadas, A. N. D., Giménez, D., Quiroz, R., and Protz, R., 2003, "Multifractal Characterization of Soil Pore Systems," Soil Sci. Soc. Am. J., **67**(5), p. 1361.
[30] Stanczak, G., 2014, "Fractal Analysis of the Pore Space in Sandstones as Derived From Mercury Porosimetry and Image Analysis," International Multidisciplinary Microscopy Congress, Antalya, Turkey, Oct. 10–13, Vol. 154.
[31] Yang, Y., Yang, H., Tao, L., Yao, J., Wang, W., Zhang, K., and Luquot, L., 2019, "Microscopic Determination of Remaining Oil Distribution in Sandstones With Different Permeability Scales Using Computed Tomography Scanning," ASME J. Energy Resour. Technol., **141**(9), p. 092903.
[32] Cnudde, V., Boone, M., Dewanckele, J., Dierick, M., Van Hoorebeke, L., and Jacobs, P., 2011, "3D Characterization of Sandstone by Means of X-ray Computed Tomography," Geosphere, **7**(1), pp. 54–61.
[33] De Boever, W., Derluyn, H., Van Loo, D., Van Hoorebeke, L., and Cnudde, V., 2015, "Data-Fusion of High Resolution X-ray CT, SEM and EDS for 3D and Pseudo-3D Chemical and Structural Characterization of Sandstone," Micron, **74**, pp. 15–21.
[34] Munawar, M. J., Lin, C., Cnudde, V., Bultreys, T., Dong, C., Zhang, X., De Boever, W., Aleem Zahid, M., and Wu, Y., 2018, "Petrographic Characterization to Build an Accurate Rock Model Using Micro-CT: Case Study on Low-Permeable to Tight Turbidite Sandstone From Eocene Shahejie Formation," Micron, **109**, pp. 22–33.
[35] Chen, W.-S., Yuan, S.-Y., and Hsieh, C.-M., 2003, "Two Algorithms to Estimate Fractal Dimension of Gray-Level Images," Opt. Eng., **42**(8), p. 2452.
[36] Li, A., Ding, W., Jiu, K., Wang, Z., Wang, R., and He, J., 2018, "Investigation of the Pore Structures and Fractal Characteristics of Marine Shale Reservoirs Using NMR Experiments and Image Analyses: A Case Study of the Lower Cambrian Niutitang Formation in Northern Guizhou Province, South China," Mar. Pet. Geol., **89**(Part 3), pp. 530–540.
[37] Vicente, J., Wyart, Y., and Moulin, P., 2013, "Characterization (Two-Dimensional-Three-Dimensional) of Ceramic Microfiltration Membrane by Synchrotron Radiation: New and Abraded Membranes," J. Porous Media, **16**(6), pp. 537–545.
[38] Mehmani, A., and Prodanović, M., 2014, "The Effect of Microporosity on Transport Properties in Porous Media," Adv. Water Resour., **63**, pp. 104–119.
[39] Sagan, H., 1994, *Space-Filling Curves*, S. Shekhar and H. Xiong, eds., Springer-Verlag, Berlin, pp. 9–30.
[40] Vicsek, M., and Vicsek, T., 1997, "Aggregation Models of Fractal Growth," Centrum Voor Wiskunde En Informatica Quarterly, **10**(2), pp. 153–178. http://citeseerx.ist.psu.edu/viewdoc/summary?doi=10.1.1.56.8749
[41] Zhao, W., Zhang, Y., Xu, B., Li, P., Wang, Z., and Jiang, S., 2018, "Multiple-Relaxation-Time Lattice Boltzmann Simulation of Flow and Heat Transfer in Porous Volumetric Solar Receivers," ASME J. Energy Resour. Technol., **140**(8), p. 082003.
[42] Xia, Y., Cai, J., Wei, W., Hu, X., Wang, X., and Ge, X., 2017, "A New Method for Calculating Fractal Dimensions of Porous Media Based on Pore Size Distribution," Fractals, **26**(01), p. 1850006.
[43] Cai, J., Luo, L., Ye, R., Zeng, X., and Hu, X., 2015, "Recent Advances on Fractal Modeling of Permeability for Fibrous Porous Media," Fractals, **23**(01), p. 1540006.